

Research Paper

Dosimetric evaluation of radionuclides for VCAM-1-targeted radionuclide therapy of early brain metastases

Nadia Falzone^{1*}✉, Nicole L. Ackerman^{2*}, Liset de la Fuente Rosales³, Mario A. Bernal³, Xiaoxuan Liu¹, Sarah GJA Peeters¹, Manuel Sarmiento Soto¹, Aurélien Corroyer-Dulmont^{1,4}, Myriam Bernaudin⁴, Elisa Grimoin⁴, Omar Touzani⁴, Nicola R. Sibson¹, Katherine A. Vallis¹

1. CR-UK/MRC Oxford Institute for Radiation Oncology, Department of Oncology, University of Oxford, Oxford, United Kingdom;
2. Department of Physics and Astronomy, Agnes Scott College, Decatur, GA, United States of America;
3. Departamento de Física Aplicada, Instituto de Física "Gleb Wataghin", UNICAMP, Campinas, Brazil;
4. Normandie Univ, UNICAEN, CEA, CNRS, ISTCT/CERVOxy group, Caen, France.

* Joint first authors

✉ Corresponding author: Nadia Falzone, PhD, CRUK/MRC Oxford Institute for Radiation Oncology, Department of Oncology, University of Oxford, Old Road Campus Research Building, Off Roosevelt Drive, Oxford. OX3 7LJ. T: +44 (0)1865 225841 F: +44 (0) 1865 857127 Email: nadia.falzone@oncology.ox.ac.uk

© Ivyspring International Publisher. This is an open access article distributed under the terms of the Creative Commons Attribution (CC BY-NC) license (<https://creativecommons.org/licenses/by-nc/4.0/>). See <http://ivyspring.com/terms> for full terms and conditions.

Received: 2017.08.03; Accepted: 2017.10.02; Published: 2018.01.01

Abstract

Brain metastases develop frequently in patients with breast cancer, and present a pressing therapeutic challenge. Expression of vascular cell adhesion molecule 1 (VCAM-1) is upregulated on brain endothelial cells during the early stages of metastasis and provides a target for the detection and treatment of early brain metastases. The aim of this study was to use a model of early brain metastasis to evaluate the efficacy of α -emitting radionuclides, ^{149}Tb , ^{211}At , ^{212}Pb , ^{213}Bi and ^{225}Ac ; β -emitting radionuclides, ^{90}Y , ^{161}Tb and ^{177}Lu ; and Auger electron (AE)-emitters ^{67}Ga , ^{89}Zr , ^{111}In and ^{124}I , for targeted radionuclide therapy (TRT).

METHODS: Histologic sections and two photon microscopy of mouse brain parenchyma were used to inform a cylindrical vessel geometry using the Geant4 general purpose Monte Carlo (MC) toolkit with the Geant4-DNA low energy physics models. Energy deposition was evaluated as a radial function and the resulting phase spaces were superimposed on a DNA model to estimate double-strand break (DSB) yields for representative β - and α -emitters, ^{177}Lu and ^{212}Pb . Relative biological effectiveness (RBE) values were determined by only evaluating DNA damage due to physical interactions.

RESULTS: ^{177}Lu produced 2.69 ± 0.08 DSB per GbpGy, without significant variation from the lumen of the vessel to a radius of 100 μm . The DSB yield of ^{212}Pb included two local maxima produced by the 6.1 MeV and 8.8 MeV α -emissions from decay products, ^{212}Bi and ^{212}Po , with yields of 7.64 ± 0.12 and 9.15 ± 0.24 per GbpGy, respectively. Given its higher DSB yield ^{212}Pb may be more effective for short range targeting of early micrometastatic lesions than ^{177}Lu .

CONCLUSION: MC simulation of a model of early brain metastases provides invaluable insight into the potential efficacy of α -, β - and AE-emitting radionuclides for TRT. ^{212}Pb , which has the attributes of a theranostic radionuclide since it can be used for SPECT imaging, showed a favorable dose profile and RBE.

Key words: radionuclides, VCAM-1, brain metastases

Introduction

The development of brain metastases is a frequent complication of several common cancers. For

example, it occurs in ~30% of breast cancer patients, with a particularly high risk among patients with

triple-negative and human epidermal growth factor receptor 2 (HER2)-positive disease [1]. The management of brain metastases is complex and, depending on the clinical situation, may include surgical resection, whole-brain radiation therapy (WBRT), stereotactic radiosurgery (SRS), chemotherapy and molecularly targeted agents or combinations of these. Patients with multiple metastases, uncontrolled systemic disease, and poor functional status are typically treated with WBRT alone, whereas surgery and SRS may be used to achieve local control in those patients with single or oligo-metastases and good functional status [2]. Surgery and WBRT are sometimes used in conjunction with chemotherapy, anti-estrogen or HER2-targeted therapies depending on patient and tumor characteristics [3-7]. Despite these therapeutic options, brain metastases remain a significant cause of morbidity and mortality among breast cancer patients and novel approaches to their management are needed.

Targeted radionuclide therapy (TRT) allows precise delivery of systemically administered radioactivity to disseminated cancer cells. Unlike conventional, non-radiolabeled targeted therapies, which only affect cells that express the relevant molecular target [8], TRT may damage tumour cells even if they lack the specific tumor-associated antigen or receptor through cross-fire or bystander effects [9]. This unique feature extends the tumoricidal capacity of TRT beyond the physical location of the radionuclide [10]. An added advantage of this therapy is that many of the α -, β - and Auger electron (AE)-emitting radionuclides used for TRT permit simultaneous diagnostic radioimaging through emission of γ and annihilation photons that can be detected using single photon emission computed tomography (SPECT) or positron emission tomography (PET). The use of TRT in the treatment of primary brain tumors or metastasis has been reported previously. ^{131}I -labeled L19SIP (radretumab) is a small immunoprotein directed against the extracellular-B domain of fibronectin, which is present in the extracellular matrix surrounding newly formed blood vessels, such as in solid tumors. L19SIP has shown therapeutic benefit in patients with brain metastases originating from non-small cell lung cancer or breast carcinoma [11, 12]. This radiopharmaceutical is being developed as a treatment in combination with WBRT and as a companion PET imaging agent; ^{124}I -labeled L19SIP is used to inform dosimetry of the therapeutic [13]. TRT has also been described in the treatment of high grade gliomas. For example, substance P, a ligand of the transmembrane receptor neurokinin

type-1 (NK-1), which is consistently overexpressed in gliomas, has been labeled with ^{90}Y , ^{177}Lu or ^{213}Bi , and has shown little toxicity and improved neurologic status in clinical trials [14, 15]. Antitenascin antibodies labelled with ^{131}I , ^{90}Y or ^{211}At have been instilled into resection cavities following surgery for malignant central nervous system (CNS) tumors [16-18]. Both β - (^{131}I and ^{90}Y) and α - (^{211}At) emitting constructs were well tolerated with little associated toxicity, promising antitumor benefit in patients.

It is known that vascular cell adhesion molecule 1 (VCAM-1) is highly expressed on endothelial cells during the initial stages of metastatic seeding to the brain [19], and plays a key role in tumor cell adhesion to the vascular endothelium and subsequent transendothelial migration [19, 20]. VCAM-1 could, therefore, act as a target for TRT of early stage brain metastases. Indeed, a radiolabeled VCAM-1 specific peptide has been identified as a viable imaging probe in a mouse model of ovarian cancer peritoneal metastasis [21]. Therefore, a theranostic radionuclide targeted to VCAM-1 could be used to simultaneously image and treat early brain metastases. However, to avoid normal brain cell damage and associated loss of brain function, the range of the particulate emissions from the radionuclide used should reflect the extent of metastasis penetration into the brain parenchyma [22] while still providing a high absorbed radiation dose and uniform dose distribution [23]. Thus, a biologically informed Monte Carlo (MC) model could provide invaluable insights into the selection of a radionuclide with a favourable dose profile.

The choice of therapeutic radionuclides is often limited by commercial availability and chemical suitability for attachment to a particular carrier molecule. In this paper we evaluate the merits of commercially available radionuclides for early brain metastasis targeting, by considering their absorbed dose profiles and DNA damaging potential in a geometric model that is based on information derived from a murine model of brain metastases (Fig. 1). Event-by-event MC simulation of the complete radiation spectra of α -emitting radionuclides, namely ^{149}Tb , ^{211}At , ^{212}Pb , ^{213}Bi and ^{225}Ac ; β -emitting radionuclides, ^{90}Y , ^{161}Tb and ^{177}Lu ; and AE-emitters ^{67}Ga , ^{89}Zr , ^{111}In and ^{124}I , affords exquisite detail of their absorbed dose profiles and obviates the need to evaluate all of their effects individually in animal models. Using an atomistic model to simulate radiation-DNA interaction [24, 25], we are then able to evaluate the merits of the most favourable radionuclides for potential use in the treatment of early brain metastasis.

Material and Methods

In Vivo Models

A GFP-tagged sub-clone of a triple negative human breast carcinoma cell line that preferentially metastasizes to the brain, MDA231BR, was used [19, 26, 27]. Briefly, female SCID mice ($n = 3$), 7–8 weeks old, were anesthetized and received intra-cardiac injections of 1×10^5 MDA231BR cells in 100 μL PBS. At 21 days after tumour cell injection, animals were terminally anaesthetized with 0.3 mL sodium pentobarbitone and transcardially perfusion-fixed using intra-cardiac injections of 0.9% heparinised saline followed by 10 mL of periodate lysine paraformaldehyde with 0.01% glutaraldehyde. Brains were cryoprotected, frozen in isopentane and 10–20 μm thick sections were cut. All *in vivo* experiments were approved by the UK Home Office and the French regional committee on animal ethics (CENOMEXA).

Immunohistochemistry

The expression of VCAM-1 and CD31, a marker of endothelial cells, were assessed in brain tissue as previously described [19, 20]. Briefly, sections were rehydrated in phosphate-buffered saline (PBS;

Thermo Fisher Scientific, UK; pH 7.4), quenched with 1% hydrogen peroxide (Sigma Aldrich, UK) in methanol and blocked in 10% normal goat serum for VCAM-1 expression or normal horse serum for CD31. Primary antibody was incubated overnight at 4° C, using 1:250 dilution for VCAM-1 (rat anti-mouse, Cambridge Bioscience, 1510-14) or 1:100 dilution for CD31 (goat anti-mouse, Bio-Techne R&D, AF3628). Samples were then incubated for 1 h at room temperature using a biotinylated goat anti-rat (1:100, vectorlabs, CA, USA) or biotinylated horse anti-goat secondary antibody (1:200, vectorlabs). After amplification using the ABC reaction, staining was detected using standard DAB/hydrogen reaction. Sections were counterstained using cresyl violet and mounted using DPX mounting solution (Thermo Fisher Scientific, UK). Slides were scanned using an Aperio brightfield scanner (Leica Biosystems) and analysed using ImageScope®. Histologic sections of mouse brain parenchyma were used to measure the diameter of CD31-stained blood vessels and the depth of cancer cell infiltration into brain tissue. These data were used to generate a geometric model for MC simulation that reflected the dimensions of brain metastases at 21 days following intracardiac injection in the MDA231BR model.

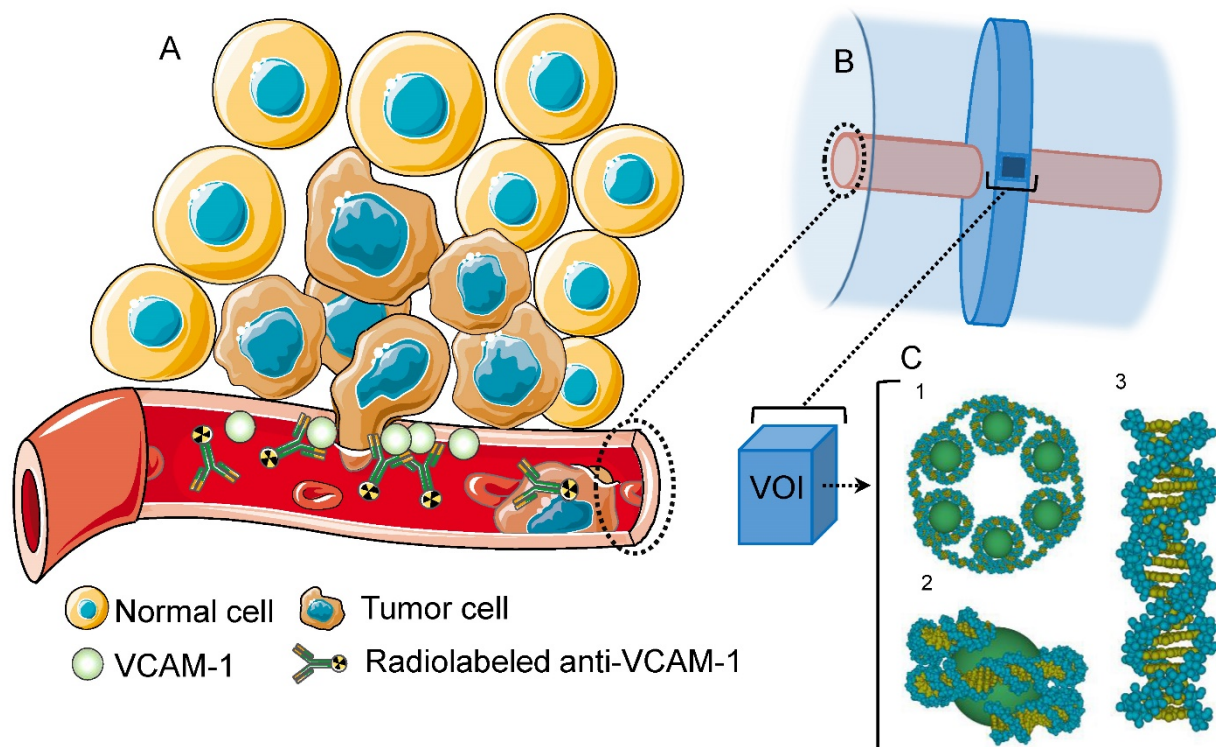


Figure 1. (A) VCAM-1 mediated cancer infiltration into the brain parenchyma; anti-VCAM-1 radionuclide immunoconstruct binds VCAM-1 and irradiates the metastasis. (B) Geant4 geometry: The inner cylinder (red) depicts the vessel and the outer cylinder (blue) the volume in which energy deposition was recorded. The disk around the vessel shows the volume where Geant4-DNA physics models were applied and (C) contains the atomistic geometrical model of the B-DNA configuration for DNA [25]. Each VOI is filled with 30 nm chromatin fibers (5.47 Gbp). These are formed by a helix with 6 nucleosomes/turn. Two adjacent nucleosomes are bound by a DNA fragment containing 46 bp. (1) Fragment of the 30 nm chromatin fiber containing 6 nucleosomes (one helix pitch). (2) Two helicoidal loops with 77 bp each folded around a sphere simulating a histone. (3) Sample of a straight fragment of the B-DNA double helix containing 20 bp.

Two Photon microscopy

Animals ($n = 3$) were injected intracardially with GFP-positive MDA231BR cells. After 21 days, animals were anesthetized using isoflurane (5% in an O_2/N_2O mixture for induction and 1.0-1.5% during surgery). Analgesic (tolfedine, 4 mg/kg), was administered subcutaneously. The rectal temperature was monitored and maintained at 37.5°C using a heating pad. A circular region over the somatosensory cortex (2 x 2 mm in size) was gently thinned to ~50 μm with a high speed drill. The thinned region was coated with a drop of cyanoacrylate glue to facilitate a viewing window [28]. *In vivo* two-photon imaging was performed on a Leica DM6000 stand (CYCERON biomedical imaging platform) with a 25x/0.95 water HXC IRAPO objective and laser excitation wavelength centered at 900 nm. Animals were positioned during microscopy using a custom built cradle and received an intravenous (i.v.) injection of tetramethyl rhodamine isothiocyanate (TRITC-dextran, 70 kDA, 10 mg/mL) (Sigma-Aldrich) to visualize the vascular compartment.

Monte Carlo Modeling – Geant4-DNA

Monte Carlo modeling of radiation transport was performed using the Geant4.10.02.p02 toolkit [29]. The coupled transport of charged particles and photons were evaluated for α -emitting radionuclides (^{149}Tb , ^{211}At , ^{212}Pb , ^{213}Bi and ^{225}Ac), β -emitting radionuclides (^{90}Y , ^{161}Tb and ^{177}Lu) and AE-emitters (^{67}Ga , ^{89}Zr , ^{111}In and ^{124}I). Energy losses were tallied when the complete decay spectra of each radionuclide, including daughters in the various α decay schemes, interacted with liquid water (density scaled to 1.06 g/cm³). Each energy deposit was associated with a particle produced in the decay, differentiating electron ionization events downstream of α -particles or electrons produced from the initial decay. The geometry consisted of a cylinder representing a blood vessel with point sources randomly distributed on its luminal surface, simulating binding of a radiolabeled anti-VCAM-1 antibody to the VCAM-1 receptor (Fig. 1).

Energy deposits were recorded in a 3.5 μm thick virtual disk, centred with respect to the vessel volume, extending from the vessel wall to a radius of 110 μm (Fig. 1B). This geometry was specifically chosen such that recorded energy deposition could be superimposed on an atomistic resolution DNA geometrical model contained in a rectangular prism (Fig. 1C) [30]. The Geant4-DNA models were used for electromagnetic processes involving electron energies < 1 MeV in this volume as well as a buffer region extending at least 3.0 μm in all directions. Throughout

the entire simulation, the Geant4-DNA processes were enabled for helium, single-ionized helium (α^+), and doubly-ionized helium (α) particles. The Livermore electromagnetic models were used for γ -rays in the whole simulation volume, for high energy electrons in the target plus buffer region, and for all electrons outside this region. The secondary electron production threshold was set to 990 eV outside the target plus buffer region, which corresponds to a range of approximately 1 μm . Electrons were tracked down to an energy of 8.0 eV, at which point the energy was deposited locally. Energy deposition in this geometry was converted to absorbed dose (Gy) and binned at 1 μm intervals. Statistical uncertainties were calculated by dividing the simulation results into batches (5 for the Geant4 simulations and 10 for the DNA damage simulations) and calculating the standard deviation of the results. The effect of variation in vessel diameter and active vessel length (i.e., the longitudinal section of the vessel with randomly distributed point sources) on absorbed dose calculation was also considered. Cylinder diameters were 5, 10 and 15 μm and the active vessel length for a cylinder of diameter 15 μm was varied from 20 to 100 μm . The DNA strand break yields of a selected α -emitter, ^{212}Pb , and β -emitter, ^{177}Lu , were evaluated from these simulations.

To have comparable statistical uncertainties in the DSB yields for ^{177}Lu and ^{212}Pb , the number of events for ^{177}Lu was increased to achieve comparable dose. Energy deposition phase spaces for ^{177}Lu and ^{212}Pb were superimposed on the DNA geometrical model to estimate direct DSB yields, reported per unit of absorbed dose (Gy) and 10⁹ base pairs (Gbp). The DNA geometrical model was filled with chromatin fibers containing 5.47 Gbp. Each rectangular prism (3.085 x 3.085 x 3.383 μm^3) represents a volume of interest (VOI), which were spaced 5 μm apart radially within the disk. The number of VOIs varied based on the vessel radius. A single strand break (SSB) was recorded if an energy transfer greater than 8.0 eV occurs within a DNA sugar-phosphate group. A DSB was recorded if two SSB on opposed DNA strands were separated by no more than 10 bp [31]. In this study, DSB yield was used as the biological endpoint to estimate the relative biological effectiveness (RBE) of the radionuclides being investigated. RBE was determined with respect to ^{60}Co radiation, for which the DSB yield is 3.60 \pm 0.05 (per GbpGy) [32, 33].

Results

Immunohistochemistry

In total, 929 brain tissue vessels identified by CD31 immunostaining from 3 animals were analysed

(Fig. 2A). To account for variation in vessel diameter in the mouse model of brain metastasis and to provide realistic dimensions for MC simulation, vessel diameters were grouped as $< 5 \mu\text{m}$, $5\text{-}10 \mu\text{m}$, and $> 10 \mu\text{m}$, with corresponding mean \pm SD diameters measured as $4.04 \pm 0.64 \mu\text{m}$, $6.16 \pm 1.00 \mu\text{m}$ and $13.25 \pm 3.19 \mu\text{m}$. The maximal penetration of MDA231BR cells into the brain parenchyma was evaluated at day 21. In mice that received intracardiac injections of MDA231BR cells, tumors grew into the cerebral parenchyma from blood vessels with maximum penetration depths of $30.6 \mu\text{m}$, $47.8 \mu\text{m}$ and $23.2 \mu\text{m}$ from the vessel wall, for vessel diameters of $< 5 \mu\text{m}$, between 5 and $10 \mu\text{m}$, and $> 10 \mu\text{m}$ respectively (Fig. 2B). Two photon microscopy images (Fig. 2C) confirmed the penetration depths and co-optive growth of MDA231BR-GFP cells around vessels.

Dose deposition profiles

A summary of the normalized absorbed dose profiles of AE-, β - and α -emitting radionuclides as a function of distance from a vessel of diameter $15 \mu\text{m}$ and active length of $40 \mu\text{m}$ is shown in Fig. 3. The maximum penetration depth of brain metastasis as noted from the immunohistochemistry results at day 21 is $\sim 50 \mu\text{m}$ from the edge of the vessel. Thus, the dose profiles of the different radionuclides were evaluated in terms of dose deposition over this

distance from a vessel. Apart from ^{177}Lu , ^{161}Tb , and ^{67}Ga , the absorbed dose of all other electron emitters (AE and β emitters) decreased by more than 2 orders of magnitude over the first $50 \mu\text{m}$ from the vessel (Fig. 3A). The ranking order of the electron emitters from highest to lowest total dose over the $50 \mu\text{m}$ distance were ^{161}Tb , ^{177}Lu , ^{90}Y , ^{67}Ga , ^{111}In , ^{124}I and ^{89}Zr . If all of the electron-emitting radionuclides are constrained to have the same dose at the vessel (i.e., the normalized dose plot) the highest dose contribution over this distance arises from ^{177}Lu . In the $40\text{-}60 \mu\text{m}$ region the dose deposition from ^{177}Lu was comparable to that of ^{90}Y , but otherwise the normalized dose from ^{177}Lu exceeded that of ^{90}Y . On the other hand, for α -emitters (Fig. 3B), only ^{149}Tb showed a decrease greater than 2 orders of magnitude over this distance. The ranking for α -emitters was ^{225}Ac , ^{211}At , ^{212}Pb , ^{213}Bi and ^{149}Tb . ^{225}Ac imparted an absorbed dose ~ 4 times higher than the other α -emitters for most distances, since it has 4 α -particles in its decay chain. The differences between ^{211}At , ^{212}Pb , and ^{213}Bi (in terms of absolute dose) were small. The dose fall off from ^{212}Pb was the furthest from the vessel compared to all other α -emitters, since it has the most energetic α -particle component. Dose decreased by 2 orders of magnitude from the vessel to about $85 \mu\text{m}$, then another 2 orders of magnitude to $\sim 100 \mu\text{m}$.

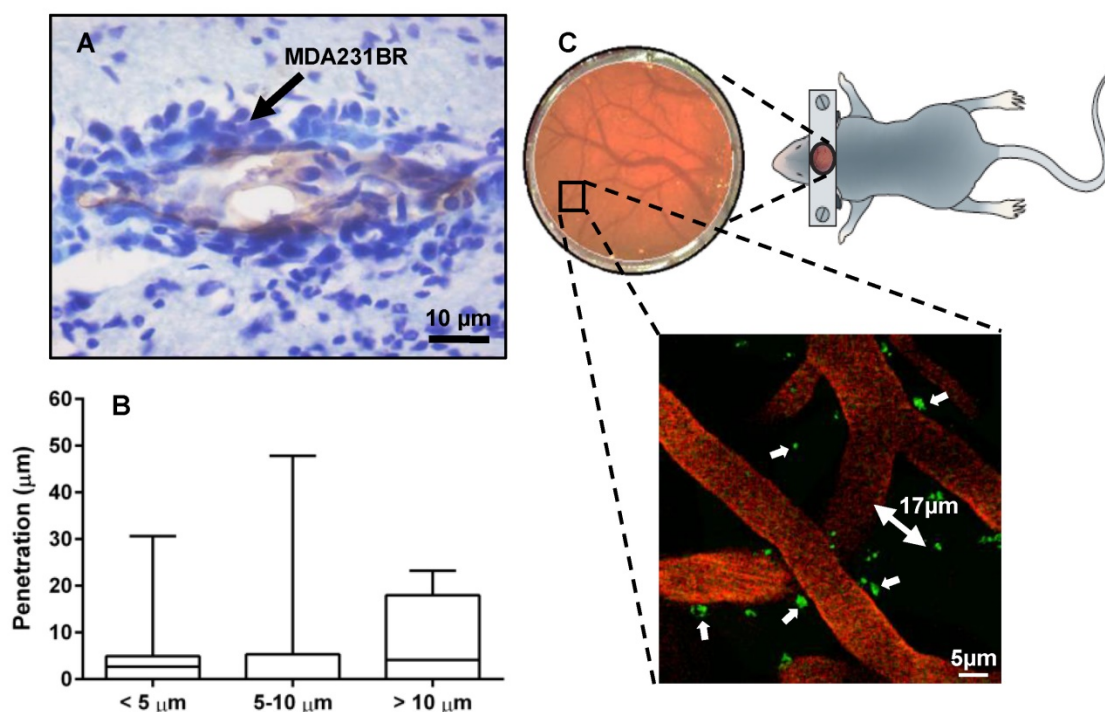


Figure 2. (A) Immunohistochemical detection of brain metastases. Photomicrograph of tumor colonies showing co-localization of VCAM-1 (brown) with brain metastasis (violet) at day 21 after intra-cardiac injection of MDA231BR cells. (B) Summary statistics of the depth of penetration of cancer cells for vessels of different diameters. Box and whiskers plots of minimum to maximum values, showing the median and SD at each vessel diameter grouping. (C) 2-Photon microscopy of brain parenchyma and vessels (seen through viewing window) showing co-optive growth (white arrows) of GFP MDA231BR cells (green) around vessels (orange - TRITC) with maximal penetration from the vessel lumen in this slice, $17 \mu\text{m}$.

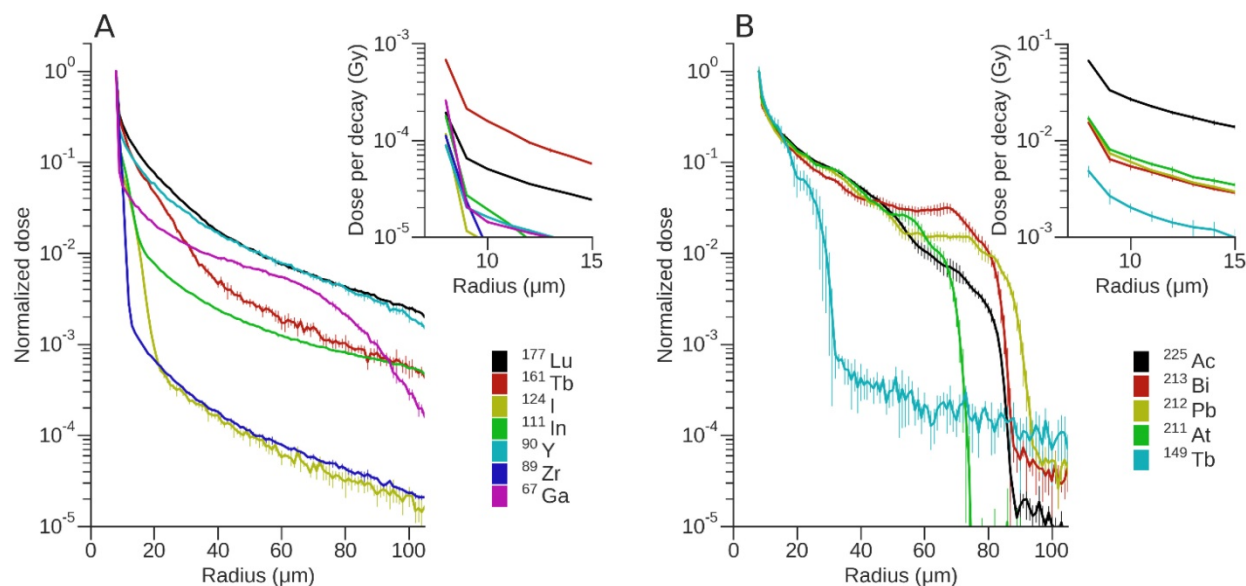


Figure 3. Absorbed dose profiles of each radionuclide for a vessel of 15 μm radius and length of 40 μm . Dose was normalised to the first bin with bin width set at 1 μm . Data points represent the average and SD of 5 runs. Absorbed dose profiles for (A) AE and β -emitting radionuclides and (B) α -emitting radionuclides. Insets show the non-normalized dose (in Gy) per event.

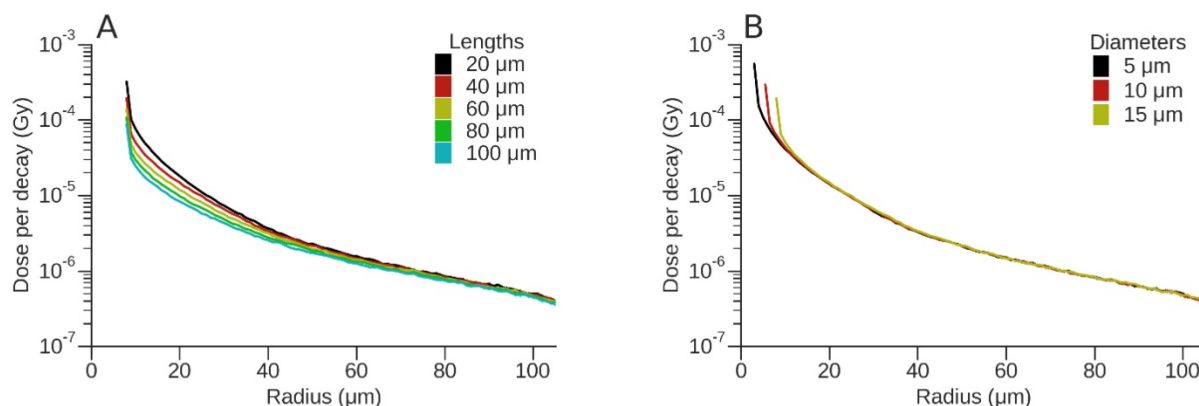


Figure 4. Dose per decay (Gy) for ^{177}Lu . (A) Variation of absorbed dose (Gy) for a 15 μm diameter vessel as a function of vessel length. (B) Variation of absorbed dose (Gy) for a vessel of length 40 μm as a function of vessel diameter.

To evaluate the effect of vessel diameter and active vessel length on absorbed dose, the dose deposition profiles for ^{177}Lu and ^{212}Pb are shown (Figs. 4 and 5). For ^{177}Lu , the dose per decay for longer vessels was lower than that of shorter vessels. For example, for vessel lengths of 20 μm and 100 μm this difference decreased from 73% at the vessel wall to 21% at a radius of 57.5 μm (50 μm from vessel wall) (Fig. 4A). Increasing vessel diameter resulted in an almost 3-fold decrease in dose per decay over the first 10 μm from the vessel wall; however, the difference was < 8% for radial distances between 20 μm and 100 μm (Fig. 4B). Similarly for ^{212}Pb , the difference between the dose per event for vessel lengths of 20 μm and 100 μm decreased from 72% at the vessel wall to 15% at a radius of 57.5 μm (Fig. 5A), while the dose per event decreased up to 3-fold from a vessel length of 20 μm to 100 μm . An increase in vessel diameter

resulted in a radial shift of dose deposition with a 59% decrease in dose per decay immediately adjacent to the vessel for the largest versus the smallest vessel radii. For greater distances the difference between the vessel diameters was typically smaller than the dose uncertainty, other than the steep fall off, which shifted in position based on the difference of diameters (Fig. 5B).

DNA strand break yield and RBE

A summary of the DSB induction potential of ^{177}Lu vs. that of ^{212}Pb is presented in Fig. 6. For ^{177}Lu (Fig. 6A), the VOI dose contribution from photons over the considered range was negligible when compared to that from electrons. The total dose and DSB yield (Fig 6C) was mostly due to the contribution of electrons (β^- -particles). On average, ^{177}Lu produced 2.69 ± 0.08 DSB per GbpGy. Over the distance

considered, contributions from major groups of electrons to DSB induction resulted in fluctuations of < 10%.

To fully understand the DSB profile of ^{212}Pb , it is necessary to consider its physical decay scheme. ^{212}Pb (10.6 h half-life) does not directly emit α -particles, but its daughters ^{212}Bi and ^{212}Po emit two α -particles during their decay. ^{212}Pb decays to ^{212}Bi via β -emission. In turn ^{212}Bi (60 min half-life) decays to stable ^{208}Pb through one of two possible paths, each of which passes through one intermediate nuclide, releasing one α -particle and one β -particle. For 36% of

the time, ^{212}Bi emits an α -particle of 6.1 MeV and decays to ^{208}Tl , which in turn decays to ^{208}Pb via β -emission. For the other 64% of the time, ^{212}Bi decays to ^{212}Po via β -emission, and ^{212}Po then decays in microseconds to ^{208}Pb by emission of an 8.8 MeV α -particle. The β -particles from ^{212}Pb itself are lower energy (573 keV) than the β -particles from ^{212}Bi (2.3 MeV) and ^{208}Tl (5 MeV), while the frequency and cumulative energy from the γ -emissions is < 12% of that from the α -particles. However a 238.6 keV γ -ray, with a 43% yield, can be exploited for imaging [34].

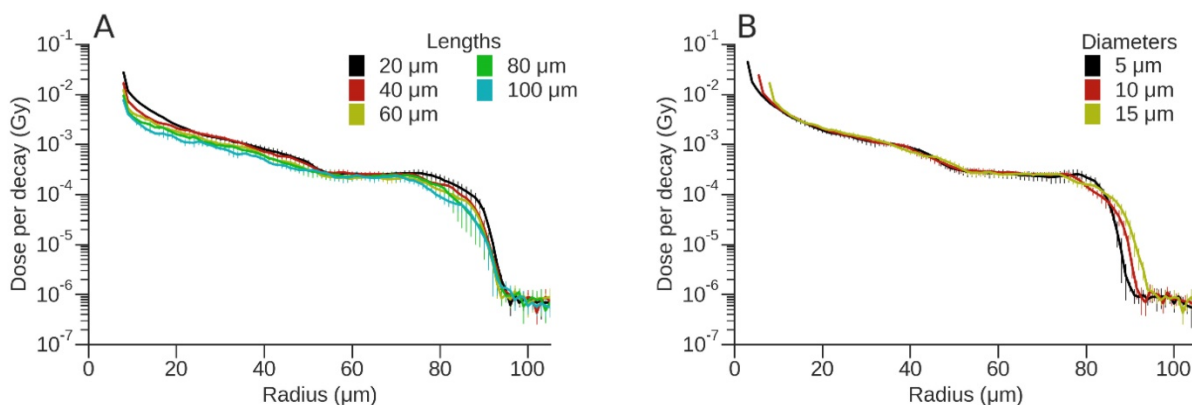


Figure 5. Dose per event (Gy) for ^{212}Pb . (A) Variation of absorbed dose (Gy) for a 15 μm diameter vessel as a function of vessel length. (B) Variation of absorbed dose (Gy) for a vessel of length 40 μm as a function of vessel diameter.

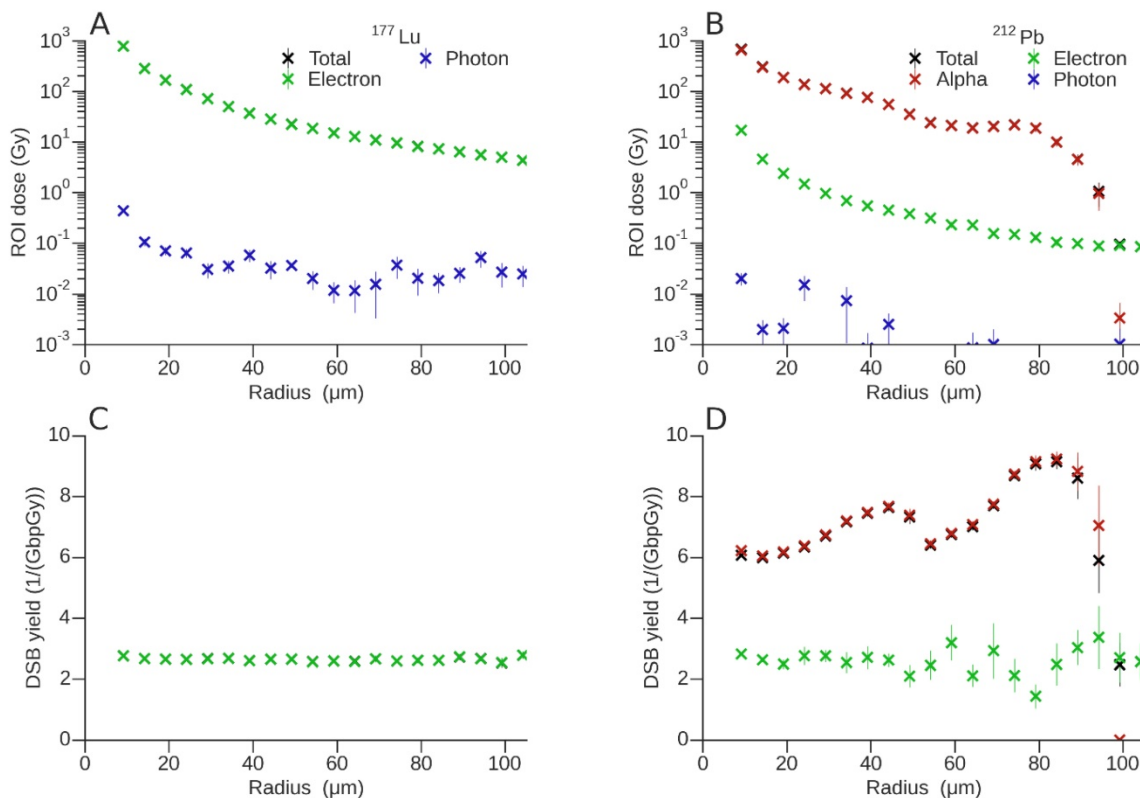


Figure 6. A summary of the total dose (Gy) delivered by (A) ^{177}Lu and (B) ^{212}Pb in each VOI as a function of radial distance from a vessel with diameter 15 μm and active vessel length of 40 μm . DSB yield (per GbpGy) for (C) ^{177}Lu and (D) ^{212}Pb . Both the dose and DSB break yields were discriminated according to the associated primary decay particle, however contributions from electrons (green) and α -particles (red) may be superimposed on the total yield (black).

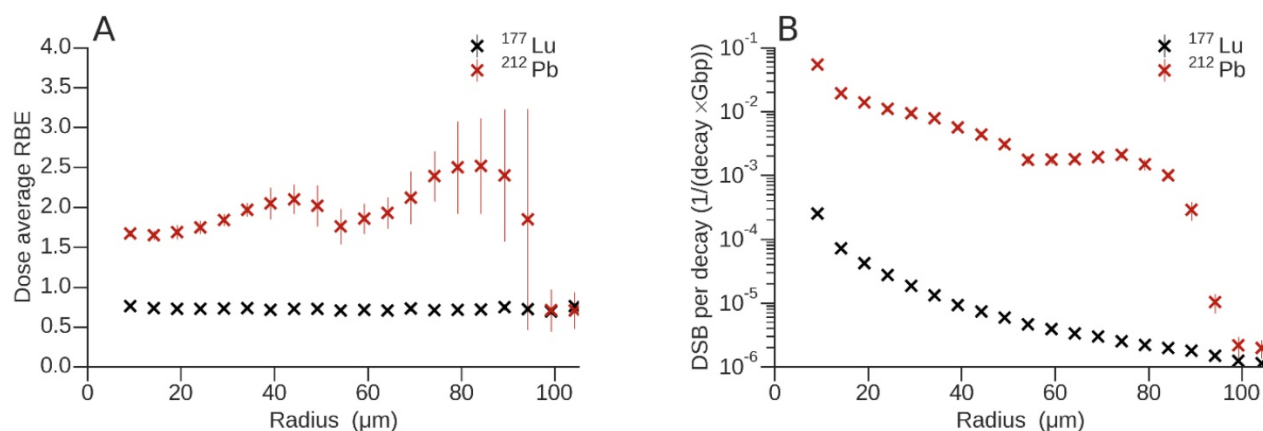


Figure 7. (A) Dose-average relative biological effectiveness for ¹⁷⁷Lu and ²¹²Pb. **(B)** Total number of DSB per decay and Gbp of ¹⁷⁷Lu and ²¹²Pb as a function of radius.

As would be predicted, the main contribution to the VOI dose from the decay of ²¹²Pb was due to the 6.1 and 8.8 MeV α -emissions from ²¹²Bi and ²¹²Po respectively (Fig. 6B). Electron doses are about two orders of magnitude lower than dose attributable to α -particles and decrease exponentially on a log scale with distance. As shown in Fig. 6B, 6D, and 7B, the dose/DSB from the electrons continued on smoothly past 100 μm , but at orders of magnitude lower than dose/DSB due to α -particles. The contribution from photons to the dose and DSB yield (Fig. 6D) was negligible and the associated uncertainties were very high. For this reason, the contribution from photons was omitted from the DSB plot. The VOI dose fluctuated with radial distance, with two local maxima observed at $\sim 40 \mu\text{m}$ and $\sim 80 \mu\text{m}$. These two regions are most evident in the DSB yields shown in Fig 6D. The peaks can be explained by the presence of the two α -particles arising from the decay of ²¹²Bi and ²¹²Po, with projected ranges of 50.1 μm and 91.0 μm and associated DSB yields per GbpGy of 7.64 ± 0.12 and 9.15 ± 0.24 respectively. It is important to note that the observed maxima are a consequence of the superposition of multiple Bragg peaks resulting from isotropically emitted α -particles on the vessel wall, and not a simple projection of ranges. DSB yields for electrons also show a very complex behaviour since there are many β and Auger components in the decay spectrum with different associated ranges. As a result, the electron DSB yield changes with distance from the vessel wall.

Estimated RBE values were determined by only evaluating DNA damage due to physical interaction of the radionuclides in question. This was done in a consistent way, using the same biophysical model for the isotopes studied. The RBE obtained for each particle type at a given distance from the vessel axis was weighted by the corresponding dose fraction (Fig. 7A). For ¹⁷⁷Lu, the contribution of electrons only,

and for ²¹²Pb the contributions of electrons and α -particles, were considered. In contrast to ²¹²Pb, the dose-average RBE for ¹⁷⁷Lu was lower than 1 (0.73 ± 0.02), which means that electrons emitted during this decay have a RBE lower than that of ⁶⁰Co. In addition, this was verified for photons where an RBE = 1 was obtained for the first 4 data points that had acceptable uncertainties (data not shown). The presence of α -particles in the ²¹²Pb spectrum produced an appreciable departure of the dose-average RBE from 1, i.e., 2.10 ± 0.18 and 2.52 ± 0.60 , mainly around the maxima as a result of the superposition of the Bragg peaks. To appreciate the difference in DSB yield between ¹⁷⁷Lu and ²¹²Pb, the total number of DSB per decay and Gbp are shown in Fig. 7B. The DSB yield of ²¹²Pb per decay varies as a function of linear energy transfer (LET) and radial distance from the vessel. The DSB yield per decay ratio between ²¹²Pb and ¹⁷⁷Lu increases to 607.34 ± 60.40 and 826.09 ± 102.11 at the local maxima produced by the 6.1 MeV and 8.8 MeV α -emissions from ²¹²Bi and ²¹²Po respectively.

Discussion

The upregulation of cellular adhesion molecules on the endothelium of cerebral blood vessels, which results from tumor cell extravasation into the brain parenchyma, presents a promising biomarker for diagnosis and therapy [21, 35]. In particular, the use of radionuclide-based theranostic agents directed against adhesion molecules is an attractive prospect. However, extensive *in vivo* experimentation to elucidate which radiopharmaceutical could potentially offer the best dose-profile and therapeutic effect for this distinctive tumour morphology would be both time consuming and costly. These obstacles can be overcome, and the most promising radionuclides selected for further study, through the use of MC simulations applied to models that accurately represent the architecture of brain

metastases. In the clinic, brain metastases frequently show a co-optive growth pattern irrespective of the primary tumour type and grow circumferentially around blood vessels [36]. The preclinical *in vivo* model MDA213BR, used in the current study, is entirely consistent with this pattern of growth. Realistic representations of MDA231BR metastases were constructed for MC simulation, reflecting the co-optive growth pattern and the depth of penetration of cancer cells as determined by immunohistochemistry and live 2-photon imaging (Fig. 2). Simulations were performed to evaluate the dose profiles of a panel of radionuclides. It is clear from the dose profiles (Fig. 3A and B) that the α -emitters offer an advantage over β - and AE-emitters. Interestingly, the normalized dose profile of ^{67}Ga compared favourably with that of ^{90}Y and ^{177}Lu . However, the very low dose imparted by the AE-emitting nuclides ^{89}Zr and ^{124}I precludes them as therapeutic radionuclides in this situation but would make them suitable for PET imaging purposes. ^{177}Lu and ^{212}Pb were then selected for further comparison and simulation as they showed the most uniform deposition of dose over 50 μm from the vessel wall, while ^{212}Pb showed the furthest penetration ($\sim 100\ \mu\text{m}$).

A vessel diameter of 15 μm , at the upper end of the range for venous radii in mouse brain, was chosen for MC simulation to facilitate direct comparison with analogous vessel diameters in human brain (median range 16–32 μm) [37]. In fact, a change in vessel radius had only a minor effect on dose profiles as a function of radial distance for the two radionuclides chosen for in-depth study, ^{177}Lu and ^{212}Pb (Fig. 4 and 5). Furthermore, a 40 μm active vessel length was used for MC simulation although tumor growth was observed in up to 5 consecutive histology sections (section thickness of 20 μm – data not shown). This choice was informed not only by computation time, but also as a direct result of the simulation results (Fig. 4 and 5) where varying active vessel length due to the symmetry in the geometry did not greatly affect the dose profiles of ^{177}Lu and ^{212}Pb . In addition, as the dose measurement was limited to a disk of width 3.5 μm to enable direct comparison with the dose measurement in the atomic DNA geometry model, the variation of dose for ^{177}Lu and ^{212}Pb was also measured over an active vessel length of 100 μm . Dose per decay showed a slight decrease at the edge of the active vessel due to the lack of charged particle equilibrium (Fig. S1). For both ^{177}Lu and ^{212}Pb , dose decreased by 25% from the mid-point to the end of the active vessel. However the initial falloff for ^{177}Lu was slightly faster compared with that of ^{212}Pb . The geometric model that was used captures the salient

features of brain vasculature and the results of simulations were robust to changes in geometry. We infer that our results can be generalized from the mouse-model measurements to the human scale relevant to a clinical scenario.

For theranostic purposes, the dose imparted per decay by α -emitting ^{212}Pb was typically two orders of magnitude higher than for β -emitting ^{177}Lu and this translated into higher DNA damage yields (Fig. 6). The short path length of α -particles render them particularly suitable for the treatment of micro-metastases or neoplastic disease that is present as single layers or sheets of cells on compartment surfaces [38]. High-LET radiation like α -particles produce dense ionizations along a linear track and generate multiply damaged sites in DNA. This is reflected in the higher DSB yields obtained for ^{212}Pb (Fig. 6D) when compared to ^{177}Lu (Fig. 6C). DSB yield (per GbpGy) for the former can be up to three times higher than for the latter. Supplementary Fig. S2 shows the total strand break (TSB) yield, which is the total number of SSB produced by ^{177}Lu or ^{212}Pb , including those leading to DSB. As shown by others, SSB depends weakly on the incident radiation quality [39, 40]. Thus, regardless of the type of primary particle and its associated energy, a similar number of SSB per unit absorbed dose and base pair are produced. This, however, does not translate into the same RBE since the number of SSB that lead to DSB tends to increase with particle LET.

The biophysical model used in the current study shows that ^{177}Lu has a dose-average RBE lower than 1 (0.73 ± 0.02), which means that it is less effective than ^{60}Co radiation (the reference quality used). Although the associated photons yielded an RBE = 1, they only had a negligible impact on the dose-averaged RBE. Indeed, the calculated RBE based on DSB yields from physical damage only is in good agreement with an experimentally determined RBE of 1 for ^{177}Lu -DOTATOC using ^{137}Cs γ -radiation as the reference radiation [41]. On the other hand, the RBE of ^{212}Pb varied with radial distance and increased to 2.10 ± 0.18 and 2.52 ± 0.60 at the local maxima of the 6.1 MeV and 8.8 MeV α -emissions from ^{212}Bi and ^{212}Po respectively. These values yield a relative $^{212}\text{Pb}/^{177}\text{Lu}$ RBE of 2.87 and 3.45, respectively. The RBE of α -particles ranges from 2 to 7, and therefore, α -particle irradiation is 2–7 times more therapeutically effective, or toxic, per unit of absorbed dose than photons or electron [38, 42, 43]. Furthermore, DSB yields per decay for ^{212}Pb varies with depth and LET and can be up to two orders of magnitude higher than those for ^{177}Lu at the local maxima of the α -emissions from ^{212}Bi and ^{212}Po . This new metric (DSB yield per decay), could be clinically

more informative than DSB yield per unit of absorbed dose, since the former can be directly estimated from the administered activity and does not require convoluted dose calculations.

Considering the favorable dose profile and DNA damage yields of ^{212}Pb , it is a good potential candidate for TRT in early brain metastasis treatment and imaging. It has an intermediate physical half life of 10.64 h compatible with clinical use [44] and emits γ -rays suitable for SPECT [45]. Furthermore, it is a practical choice because it is produced in a generator ($^{224}\text{Ra}/^{212}\text{Pb}$ generator), and stable chelation is possible using TCMC (2-(4-isothiocyanatobenzyl-1,4,7,10-tetraaza-1,4,7,10-tetra-(2-carbamoylmethyl)-cyclododecane) [46]. Meredith and co-workers recently demonstrated the efficacy of intraperitoneal ^{212}Pb -TCMC-trastuzumab in a phase I trial in ovarian cancer patients with HER-2 expressing tumors [34]. Encouragingly the treatment caused little toxicity during follow-up for 1 year [47], possibly because of the containment of the radioimmunoconjugate within the peritoneal cavity. In addition, a decrease in tumor-associated glycoprotein 72 (TAG-72) and tumor growth was associated with increasing administered radioactivity. However, a potential problem when using an α -emitter with serial decay to α -emitting daughters, is that the recoil energy is sufficient to detach the daughters from the targeting vector [38]. In the case of ^{212}Pb , the mononuclear complex produced between ^{212}Pb and TCMC results in an extremely stable compound for *in vivo* use [48].

All systemically administered therapeutics, including radiopharmaceuticals, that are designed to treat brain metastases face common obstacles: the need for delivery across the blood-brain barrier (BBB) and the need to reach the molecular target in adequate concentration [49]. The issue of access to metastatic sites behind an intact BBB is being addressed using a number of different approaches. For example, Connell *et al.* demonstrated that it is possible to selectively permeabilize the BBB at metastatic sites through systemic cytokine administration, thus facilitating delivery of therapeutic agents across the BBB [50]. Similarly, a recent proof-of-concept study using convection-enhanced delivery of an AE-emitting radionuclide in an orthotopic xenograft glioblastoma model showed great promise to overcome the limitations of systemic delivery of TRTs [51]. However, the intrinsic sensitivity of tumor cells to the radio-pharmacologic agent is likely to be the most important determinant of its therapeutic success [4]. In this regard targeted α -particle therapy offers a distinct advantage.

Conclusion

The dimensions and 3D shape of early brain metastasis and their associated blood vessels were used to build an *in silico* replica. The model was designed to mimic targeting of VCAM-1, an endothelial marker of cancer cell invasion, by radioimmunoconjugates. In this respect, MC simulation has allowed selection of the radioisotope with the most suitable dose profile for treatment in a specific case, that is, early brain metastases. However, it would be possible to apply a similar approach to cancer lesions at other anatomical sites that have different morphology provided that the location of the target molecule and the physical dimensions of relevant structures such as blood vessels are known. ^{212}Pb , which has the attributes of a theranostic radionuclide since it can be used for SPECT imaging, showed a favorable dose profile and RBE.

Abbreviations

AE: Auger electron; BBB: blood-brain barrier; CNS: central nervous system; DNA: deoxyribonucleic acid; DSB: double-strand break; GFP: green fluorescent protein; HER2: human epidermal growth factor receptor 2; MC: Monte Carlo; PET: positron emission tomography; RBE: relative biological effectiveness; VOI: volume of interest; SPECT: single photon emission computed tomography; SRS: stereotactic radiosurgery; SSB: single strand break; TRT: targeted radionuclide therapy; VCAM-1: Vascular cell adhesion molecule 1; WBRT: whole-brain radiation therapy.

Acknowledgements

This work was supported by grants from Cancer Research UK (CRUK) (C5255/A15935), the Medical Research Council (MRC) (MC_PC_12004) and the CRUK Oxford Centre. This work was also supported by the Centre National de la Recherche Scientifique (CNRS), the French National Agency for Research "Investissements d'Avenir" n°ANR-11LABX0018-01 and the Conseil Régional de Normandie. M. A. Bernal and L. de la Fuente acknowledge the support received from the Conselho Nacional para o Desenvolvimento Científico e Tecnológico (CNPq), Brazil, for financing their research activities through the projects 306775/2015-8 and 190154/2013-6, respectively. S. Peeters acknowledges the support received by the Engineering and Physical Sciences Research Council (EPSRC) under Programme Grant EP/L024012/1 (OxCD3: Oxford Centre for Drug Delivery Devices).

Supplementary Material

Supplementary figures.

<http://www.thno.org/v08p0292s1.pdf>

Competing Interests

The authors have declared that no competing interest exists.

References

- Leone JP, Leone BA. Breast cancer brain metastases: the last frontier. *Exp Hematol Oncol.* 2015; 4: 33.
- Lu-Emerson C, Eichler AF. Brain metastases. *Continuum (Minneapolis).* 2012; 18: 295-311.
- Krop IE, Lin NU, Blackwell K, Guardino E, Huober J, Lu M, et al. Trastuzumab emtansine (T-DM1) versus lapatinib plus capecitabine in patients with HER2-positive metastatic breast cancer and central nervous system metastases: a retrospective, exploratory analysis in EMILIA. *Ann Oncol.* 2015; 26: 113-9.
- Lim E, Lin NU. Updates on the management of breast cancer brain metastases. *Oncology (Williston Park).* 2014; 28: 572-8.
- Niwinska A, Murawska M, Pogoda K. Breast cancer brain metastases: differences in survival depending on biological subtype, RPA RTOG prognostic class and systemic treatment after whole-brain radiotherapy (WBRT). *Ann Oncol.* 2010; 21: 942-8.
- Swain SM, Baselga J, Kim SB, Ro J, Semiglazov V, Campone M, et al. Pertuzumab, trastuzumab, and docetaxel in HER2-positive metastatic breast cancer. *N Engl J Med.* 2015; 372: 724-34.
- Swain SM, Baselga J, Miles D, Im YH, Quah C, Lee LF, et al. Incidence of central nervous system metastases in patients with HER2-positive metastatic breast cancer treated with pertuzumab, trastuzumab, and docetaxel: results from the randomized phase III study CLEOPATRA. *Ann Oncol.* 2014; 25: 1116-21.
- Gill MR, Falzone N, Du Y, Vallis KA. Targeted radionuclide therapy in combined-modality regimens. *Lancet Oncol.* 2017; 18: e414-23.
- Pouget J-P, Navarro-Teulon J, Bardies M, Chouin N, Cartron G, Pelegrin A, et al. Clinical radioimmunotherapy: the role of radiobiology. *Nat Rev Clin Oncol.* 2011; 8: 720-34.
- Enger SA, Hartman T, Carlsson J, Lundqvist H. Cross-fire doses from beta-emitting radionuclides in targeted radiotherapy. A theoretical study based on experimentally measured tumor characteristics. *Phys Med Biol.* 2008; 53: 1909-20.
- Erba PA, Sollini M, Orciuolo E, Traino C, Petrini M, Paganelli G, et al. Radioimmunotherapy with radretumab in patients with relapsed hematologic malignancies. *J Nucl Med.* 2012; 53: 922-7.
- Sauer S, Erba PA, Petrini M, Menrad A, Giovannoni L, Grana C, et al. Expression of the oncofetal ED-B-containing fibronectin isoform in hematologic tumors enables ED-B-targeted 131I-L195IP radioimmunotherapy in Hodgkin lymphoma patients. *Blood.* 2009; 113: 2265-74.
- Poli GL, Bianchi C, Virotta G, Bettini A, Moretti R, Trachsel E, et al. Radretumab radioimmunotherapy in patients with brain metastasis: a ¹²⁴I-L195IP dosimetric PET study. *Cancer Immunol Res.* 2013; 1: 134-43.
- Kneifel S, Cordier D, Good S, Ionescu MC, Ghaffari A, Hofer S, et al. Local targeting of malignant gliomas by the diffusible peptidic vector 1,4,7,10-tetraazacyclododecane-1-glutaric acid-4,7,10-triacetic acid-substance p. *Clin Cancer Res.* 2006; 12: 3843-50.
- Cordier D, Forrer F, Bruchertseifer F, Morgenstern A, Apostolidis C, Good S, et al. Targeted alpha-radionuclide therapy of functionally critically located gliomas with ²¹³Bi-DOTA-[Thi8, Met(O2)11]-substance P: a pilot trial. *Eur J Nucl Med Mol Imaging.* 2010; 37: 1335-44.
- Reardon DA, Akabani G, Coleman RE, Friedman AH, Friedman HS, Herndon JE, 2nd, et al. Salvage radioimmunotherapy with murine iodine-131-labeled antitenascin monoclonal antibody 81C6 for patients with recurrent primary and metastatic malignant brain tumors: phase II study results. *J Clin Oncol.* 2006; 24: 115-22.
- Reardon DA, Zalutsky MR, Akabani G, Coleman RE, Friedman AH, Herndon JE, 2nd, et al. A pilot study: ¹³¹I-antitenascin monoclonal antibody 81c6 to deliver a 44-Gy resection cavity boost. *Neuro Oncol.* 2008; 10: 182-9.
- Zalutsky MR, Reardon DA, Akabani G, Coleman RE, Friedman AH, Friedman HS, et al. Clinical experience with alpha-particle emitting ²¹¹At: treatment of recurrent brain tumor patients with 211At-labeled chimeric antitenascin monoclonal antibody 81C6. *J Nucl Med.* 2008; 49: 30-8.
- Soto MS, Serres S, Anthony DC, Sibson NR. Functional role of endothelial adhesion molecules in the early stages of brain metastasis. *Neuro Oncol.* 2014; 16: 540-51.
- Serres S, Mardiguian S, Campbell SJ, McAteer MA, Akhtar A, Krapitchev A, et al. VCAM-1-targeted magnetic resonance imaging reveals subclinical disease in a mouse model of multiple sclerosis. *FASEB J.* 2011; 25: 4415-22.
- Scalici JM, Thomas S, Harrer C, Raines TA, Curran J, Atkins KA, et al. Imaging VCAM-1 as an indicator of treatment efficacy in metastatic ovarian cancer. *J Nucl Med.* 2013; 54: 1883-9.
- Hindie E, Zanotti-Fregonara P, Quinto MA, Morgat C, Champion C. Dose deposits from ⁹⁰Y, ¹⁷⁷Lu, ¹¹¹In, and ¹⁶¹Tb in micrometastases of various sizes: Implications for radiopharmaceutical therapy. *J Nucl Med.* 2016; 57: 759-64.
- Champion C, Quinto MA, Morgat C, Zanotti-Fregonara P, Hindie E. Comparison between three promising β -emitting radionuclides, (67)Cu, (47)Sc and (161)Tb, with emphasis on doses delivered to minimal residual disease. *Theranostics.* 2016; 6: 1611-8.
- Bernal MA, Liendo JA. An investigation on the capabilities of the PENELOPE MC code in nanodosimetry. *Med Phys.* 2009; 36: 620-5.
- Bernal MA, Sikansi D, Cavalcante F, Incerti S, Champion C, Ivanchenko V, et al. An atomistic geometrical model of the B-DNA configuration for DNA-radiation interaction simulations. *Comp Phys Comm.* 2013; 184: 2840-7.
- Yoneda T, Williams PJ, Hiraga T, Niewolna M, Nishimura R. A bone-seeking clone exhibits different biological properties from the MDA-MB-231 parental human breast cancer cells and a brain-seeking clone in vivo and in vitro. *J Bone Miner Res.* 2001; 16: 1486-95.
- Larkin JR, Dickens AM, Claridge TD, Bristow C, Andreou K, Anthony DC, et al. Early Diagnosis of brain metastases using a biofluids-metabolomics approach in mice. *Theranostics.* 2016; 6: 2161-9.
- Shih AY, Mateo C, Drew PJ, Tsai PS, Kleinfeld D. A polished and reinforced thinned-skull window for long-term imaging of the mouse brain. *J Vis Exp.* 2012; 61: e3791-42.
- Agostinelli S, Allison J, Amako K, Apostolakis J, Araujo H, Arce P, et al. Geant4—a simulation toolkit. *Nucl Instrum Methods Phys Res A.* 2003; 506: 250-303.
- Incerti I, Baldacchino G, Bernal M, Capra R, Champion C, Francis Z, et al. The Geant4-DNA project. *Int J Model Simul Sci Comput.* 2010; 01: 157-78.
- Friedland W, Jacob P, Paretzke HG, Merzagora M, Ottolenghi A. Simulation of DNA fragment distributions after irradiation with photons. *Radiat Environ Biophys.* 1999; 38: 39-47.
- Friedland W, Jacob P, Bernhardt P, Paretzke HG, Dingfelder M. Simulation of DNA damage after proton irradiation. *Radiat Res.* 2003; 159: 401-10.
- Natale F, Rapp A, Yu W, Maiser A, Harz H, Scholl A, et al. Identification of the elementary structural units of the DNA damage response. *Nat Commun.* 2017; 8: 15760.
- Meredith R, Torgue J, Shen S, Fisher DR, Banaga E, Bunch P, et al. Dose escalation and dosimetry of first-in-human alpha radioimmunotherapy with ²¹²Pb-TCMC-trastuzumab. *J Nucl Med.* 2014; 55: 1636-42.
- Serres S, Soto MS, Hamilton A, McAteer MA, Carbonell WS, Robson MD, et al. Molecular MRI enables early and sensitive detection of brain metastases. *Proc Natl Acad Sci U S A.* 2012; 109: 6674-9.
- Berghoff AS, Rajky O, Winkler F, Bartsch R, Furtner J, Hainfellner JA, et al. Invasion patterns in brain metastases of solid cancers. *Neuro-Oncology.* 2013; 15: 1664-72.
- Jochimsen TH, Ivanov D, Ott DVM, Heinke W, Turner R, Möller HE, et al. Whole-brain mapping of venous vessel size in humans using the hypercapnia-induced BOLD effect. *NeuroImage.* 2010; 51: 765-74.
- Elggvist J, Frost S, Pouget JP, Albertsson P. The potential and hurdles of targeted alpha therapy - clinical trials and beyond. *Front Oncol.* 2014; 3: 324.
- Bernal MA. Evaluation of the mean energy deposit during the impact of charged particles on liquid water. *Phys Med Biol.* 2012; 57: 1745-57.
- Bernal MA, deAlmeida CE, Sampaio C, Incerti S, Champion C, Nieminen P. The invariance of the total direct DNA strand break yield. *Med Phys.* 2011; 38: 4147-53.
- Nayak TK, Norenberg JP, Anderson TL, Prossnitz ER, Stabin MG, Atcher RW. Somatostatin-receptor-targeted alpha-emitting ²¹³Bi is therapeutically more effective than beta(-)-emitting ¹⁷⁷Lu in human pancreatic adenocarcinoma cells. *Nucl Med Biol.* 2007; 34: 185-93.
- Friedrich T, Scholz U, Elsasser T, Durante M, Scholz M. Systematic analysis of RBE and related quantities using a database of cell survival experiments with ion beam irradiation. *J Radiat Res.* 2013; 54: 494-514.
- Graf F, Fahrner J, Maus S, Morgenstern A, Bruchertseifer F, Venkatachalam S, et al. DNA double strand breaks as predictor of efficacy of the alpha-particle emitter Ac-225 and the electron emitter Lu-177 for somatostatin receptor targeted Radiotherapy. *PLoS ONE.* 2014; 9: e88239.
- Mulford DA, Scheinberg DA, Jurcic JG. The promise of targeted α -particle therapy. *J Nucl Med.* 2005; 46 (Suppl 1): 199S-204S.
- Meredith RF, Torgue J, Azure MT, Shen S, Saddeki S, Banaga E, et al. Pharmacokinetics and imaging of ²¹²Pb-TCMC-trastuzumab after intraperitoneal administration in ovarian cancer patients. *Cancer Biother Radiopharm.* 2014; 29: 12-7.
- Baidoo KE, Milenic DE, Brechbiel MW. Methodology for labeling proteins and peptides with Lead-212 ((212)Pb). *Nucl Med Biol.* 2013; 40: 592-9.
- Meredith RF, Torgue JJ, Rozgaja TA, Banaga EP, Bunch PW, Alvarez RD, et al. Safety and outcome measures of first-in-human intraperitoneal alpha radioimmunotherapy with ²¹²Pb-TCMC-Trastuzumab. *Am J Clin Oncol.* 2016; [Epub ahead of print].
- Yong K, Brechbiel MW. Towards translation of (212)Pb as a clinical therapeutic; Getting the lead in! *Dalton Trans.* 2011; 40: 6068-76.
- Siegel T. Which drug or drug delivery system can change clinical practice for brain tumor therapy? *Neuro Oncol.* 2013; 15: 656-69.

50. Connell JJ, Chatain G, Cornelissen B, Vallis KA, Hamilton A, Seymour L, et al. Selective permeabilization of the blood-brain barrier at sites of metastasis. *J Natl Cancer Inst.* 2013; 105: 1634-43.
51. Thisgaard H, Halle B, Aaberg-Jessen C, Olsen BB, Therkelsen AS, Dam JH, et al. Highly Effective Auger-Electron therapy in an orthotopic glioblastoma xenograft model using convection-enhanced delivery. *Theranostics.* 2016; 6: 2278-91.